Cloud structure in Venus middle-to-lower atmosphere as inferred from VEX/VIRTIS 1.74 mum data

Takehiko Satoh, T. Imamura, G. L. Hashimoto, N. Iwagami, K. Mitsuyama, S. Sorahana, Pierre Drossart, Giuseppe Piccioni

Cloud structure in Venus middle-to-lower atmosphere as inferred from VEX/VIRTIS 1.74 μm data

T. Satoh,[1] T. Imamura,[1] G. L. Hashimoto,[2] N. Iwagami,[3] K. Mitsuyama,[3] S. Sorahana,[3] P. Drossart,[4] and G. Piccioni[5]

Received 8 May 2008; revised 6 October 2008; accepted 10 December 2008; published 25 April 2009.

[1] We have analyzed 1.74 μm nightside emission of Venus recorded using Visible and Infrared Thermal Imaging Spectrometer (VIRTIS) onboard European Space Agency's (ESA) Venus Express (Orbit 344, 30–31 March 2007). Attention was paid to how infrared radiance, intense at the center of the 1.74 μm "window", dims at an off-center wavelength (1.71 μm). Cloud models are required to simultaneously reproduce the emission intensity at 1.74 μm and the ratio of intensities ($I_{1.71\mu m}/I_{1.74\mu m}$). Our best-fit model (5 km vertical resolution) has located the main cloud opacity in 40–45 km altitude, lower than previous studies. This may be due to the use of CO_2 line parameters from a relatively new source (Carbon Dioxide Spectroscopy Databank) which may also be responsible for weaker continuum absorption, 5.6×10^{-9} cm^{-1} amagat^{-2}. The data are reproduced well by models of which total aerosol optical thickness is 30–50 plus subcloud haze at 30–40 km altitude. We have mapped the subcloud haze opacity (approximately 0–4) and found that the opacity basically anticorrelates with the 1.74 μm intensity. There are regions of "positive" correlation which may imply enhanced production of aerosols due to penetration of more sunlight in less cloudier regions. Venus Express, now with a capability of sensing "from the top to the bottom" of Venus cloud system, will greatly enhance our knowledge about the current status of Venus atmosphere.

Citation: Satoh, T., T. Imamura, G. L. Hashimoto, N. Iwagami, K. Mitsuyama, S. Sorahana, P. Drossart, and G. Piccioni (2009), Cloud structure in Venus middle-to-lower atmosphere as inferred from VEX/VIRTIS 1.74 μm data, *J. Geophys. Res.*, *114*, E00B37, doi:10.1029/2008JE003184.

1. Introduction

[2] Venus, often called the Earth's twin planet, is totally covered by aerosol layers. On the basis of in situ measurements by descent probes [see, e.g., *Esposito et al.*, 1983], the lowermost layer (haze) starts as low as 30 km altitude and an upper haze layer reaches up to 90 km. The main cloud deck extends from ~70 km (the level of unit optical depth as observed from the space in the ultraviolet) down to altitudes 45–50 km [*Esposito et al.*, 1997]. A substantial amount of energy absorbed within this enormous cloud system is thought to control the atmospheric dynamics and climate of Venus [*Crisp and Titov*, 1997].

[3] The top haze layer of mode 1 particles, of which effective radius (r_{eff}) is 0.3 μm, exhibits great variability both in space and time [*Kawabata et al.*, 1980; *Sato et al.*, 1996]. The upper cloud layer is dominated by mode 2 particles (r_{eff} = 1.0 μm) as discovered by the analysis of polarization of the reflected sunlight [*Hansen and Hovenier*, 1974]. Polarization data were utilized to constrain the refractive index of aerosols to ~1.45, and this has been regarded most important evidence that the aerosols, at least in the upper cloud, are likely to be droplets of sulfuric acid [*Sill*, 1972; *Young and Young*, 1973]. Mode 2 particles are, as indicated by descent probe measurements, abundant also in the middle cloud layer. Existence of much larger (mode 3) particles in the lower cloud has been inferred from Pioneer Venus LCPS experiment [*Knollenberg and Hunten*, 1980] with continuing controversy [*Toon et al.*, 1984]. Below the lower cloud is the lower haze layer [*Golovin and Ustinov*, 1982], of which composition as well as that of the lower cloud remains uncertain to date. To answer outstanding questions regarding this enormous cloud system, observations of the entire system with comprehensive coverage in time and space are essential.

[4] Discovery of near-infrared windows in the CO_2 absorption spectrum [*Allen and Crawford*, 1984] opened a new era for remote sensing. Such windows allow thermal emissions from deeper atmosphere of Venus to be remotely detected if observations are made on the night (unillumi-

[1]Institute of Space and Astronautical Science, Japan Aerospace Exploration Agency, Kanagawa, Japan.
[2]Laboratory for Earth and Planetary Atmospheric Science, Organization of Advanced Science and Technology, Kobe University, Kobe, Japan.
[3]Department of Earth and Planetary Science, Graduate School of Science, Tokyo University, Tokyo, Japan.
[4]LESIA, Observatoire de Paris, Meudon, France.
[5]INAF, Istituto di Astrofisica Spaziale e Fisica Cosmica, Rome, Italy.

0148-0227/09/2008JE003184

Figure 1. VIRTIS band 77 images acquired while the spacecraft was approaching Venus from the south in its Orbit 344 (30–31 March 2007). The south pole of Venus is below the bottom edge and the equator is over the top edge in each image. Circles in white dashed lines indicate locations of the same cloud feature. Note the saturated pixels are blacked out.

nated) hemisphere: Radiations at 1.74 and 2.3 μm windows originate primarily from 15–30 km and 26–45 km altitudes, respectively [*Kamp et al.*, 1988; *Kamp and Taylor*, 1990]. These altitudes are well below the main cloud deck so that the opacity variations within clouds appear as contrasts between brighter and darker regions.

[5] High spatial resolution maps in these windows were obtained by Near-Infrared Mapping Spectrometer (NIMS) onboard the Galileo spacecraft during its flyby of Venus in February 1990 [*Carlson et al.*, 1991; *Carlson and Taylor*, 1993]. These high-resolution maps exhibited intensity variations of about a factor 20 (at its best resolution of about 25 km) between the brightest and the darkest features in 2.3 μm window. Analyzing the NIMS data in the 1.7, 2.3, and 3.75 μm, *Grinspoon et al.* [1993] have constrained the amplitude and vertical distribution of the optical depth anomalies. Their findings include (1) the cloud opacity variations are largely confined to altitudes between 48 and 50 km and (2) mode 3 particles (r_{eff} = 3.65 μm) are primarily responsible to the cloud opacity variations.

[6] ESA's Venus Express arrived at Venus on 11 April 2006 and has been continuously observing Venus with a variety of instruments from an elongated polar orbit [*Svedhem et al.*, 2007]. Observations in the near-infrared windows (1.7, 2.3 μm, and other wavelengths) are done with the Visible and Infrared Thermal Imaging Spectrometer (VIRTIS) [*Piccioni et al.*, 2007; *Drossart et al.*, 2007]. Quality of the VIRTIS data (spatial resolution and signal-to-noise ratio) well exceeds that of NIMS. In addition, its coverage in space and time makes the VIRTIS data suitable to study spatial and temporal variability of Venus clouds, an important key to understand the evolution of Venus climate.

[7] In this paper, we investigate the aerosol distribution (vertical and horizontal) by analyzing VIRTIS-M-IR 1.74 μm window data. Because we deal with only VIRTIS-M-IR (medium-resolution infrared) data, hereafter we refer to VIRTIS-M-IR as just VIRTIS.

2. Data

2.1. Selecting VIRTIS Data Cubes for Analysis

[8] We analyze a small subset from the VIRTIS data archive, which is so chosen as to satisfy the following criteria: (1) Venus Express science case is 2 or 3, (2) VIRTIS pointing mode "nadir", and (3) VIRTIS exposure time is 18 s for each frame.

[9] The longest exposure (18 s) of VIRTIS data acquisition is favored in order that highest possible signal-to-noise ratio can be achieved even for the data off the center of the 1.74 μm window. In Figure 1, we display one of such data, acquired during Orbit 344 (30–31 March 2007). Three data cubes were acquired in Orbit 344 while the spacecraft was approaching Venus from the south in the ascending portion of the trajectory. The data cover a wide range in planetary latitudes from near the south pole to near the equator. Basic parameters such as the data acquisition time and the latitude coverage for three data cubes are summarized in Table 1.

2.2. Center and Wing of 1.74 μm Window

[10] A spectrum around the 1.74 μm window recorded in VI0344_01 data cube is shown in Figure 2. The center (i.e., the strongest signal pixel) of this window is at the band 77 with a close second at an adjacent band, 76. We pay our attention to how this strong emission (up to $\sim$0.2 W m^{-2} sr^{-1} μm^{-1} at the band center) dims as the CO_2 absorption increases for off-center wavelengths. In order to include an adequate amount of CO_2 absorption, while keeping a fair signal-to-noise ratio, we choose the band 74 as the secondary data wavelength (Figure 2). The wavelengths calculated for VIRTIS's bands 77 and 74 are given in Table 1. Note that VIRTIS's wavelength registration is temperature-dependent:

Table 1. Parameters for Orbit 344 VIRTIS-M-IR Data

	Start		Stop			Latitude			λ (μm)	
ID[a]	Date	Time	Date	Time	Science Case	Minimum	Maximum	T^b (K)	Band 74	Band 77
VI0344_00	30 March 2007	2132:32.7	30 March 2007	2306:52.5	2	−82.8°	−27.7°	156.94	1.7202	1.7487
VI0344_01	30 March 2007	2332:32.7	31 March 2007	0106:52.6	2	−66.2°	−9.3°	158.53	1.7189	1.7474
VI0344_02	31 March 2007	0132:32.8	31 March 2007	0306:52.6	2	−49.1°	−3.2°	159.15	1.7184	1.7469

[a]Data ID is in the form of orbit number_cube number.
[b]Average of 5 HK values under a keyword of M_SPECT_TEMP.

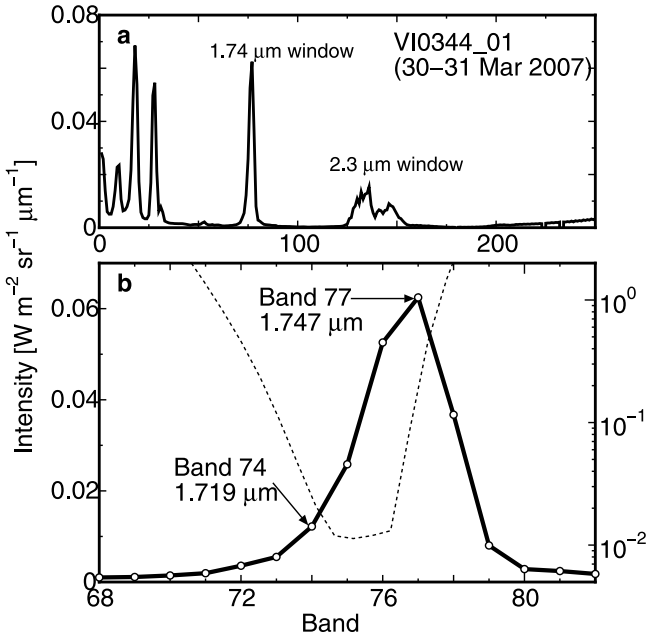

Figure 2. A spectrum of Venus nightside emission from VI0344_01 cube. (top) All near-infrared windows; (bottom) an enlarged view of the 1.74 μm window. Bands 74 and 77 used in our analysis are indicated in the bottom with their nominal wavelengths. Also shown in the bottom (dotted line) is the CO_2 opacity (optical thickness per 10 km path) for temperature and pressure at 35 km altitude. Note the horizontal offset between the intensity peak around bands 76–77 and the smallest CO_2 opacity around bands 74–76 (see text).

a 10 K higher spectrograph temperature will offset the wavelength shortward by ~0.008 μm, or 8 nm, for the 1.74 μm window. This almost compares to VIRTIS's one spectral resolution element, 9 nm.

2.2.1. Assigning Wavelengths to VIRTIS Bands

[11] The nominal wavelengths for VI0344_01 data cube are 1.747 μm (band 77) and 1.719 μm (band 74), respectively (Table 1). These assignments may, however, need some adjustments as suggested by a slight offset between the brightest signal pixels (bands 77 and 76) and wavelengths of the smallest CO_2 opacities (Figure 2).

[12] We allow a small horizontal offset to the observed spectrum so that the brightest pixels overlap with wavelengths of the smallest CO_2 opacities. By examining by eye, it is found that an offset of ~1.5 bands shortward brings the observed spectrum to a closer fit with the CO_2 opacity profile. This imply that VIRTIS's wavelength registration for VI0344_01 includes an offset of ~1.5 bands, part of which has already been noticed by the VIRTIS team (of the order of 0.01 μm) but not formularized yet. Taking this into account, we assign the wavelengths to bands 74 and 77 as follows: (1) Band 74: 1.719 μm → 1.705 μm (labeled 1.71 μm). (2) Band 74: 1.747 μm → 1.735 μm (labeled 1.74 μm). We hereafter label the band 77 intensity as $I_{1.74\mu m}$ and the band 74 intensity as $I_{1.71\mu m}$, respectively.

2.2.2. Characteristics of Wing-to-Center Ratio

[13] A set of ($I_{1.71\mu m}/I_{1.74\mu m}$) ratio images are displayed in Figures 3a–3c. We hereafter refer to this ratio as wing-to-center (W2C) ratio. Relief-like appearances of cloud edges are due to a slight vertical offset between two images. They nearly disappear when we shift the band 77 image upward by 0.35 pixels before taking a ratio (Figures 3d–3f). It has also been pointed out that VIRTIS's spectral registration is nonuniform across a frame (B. Bezard, private communication, 2008). The effect is obvious in Figures 3a–3c as systematic brightening toward the right edges. We correct

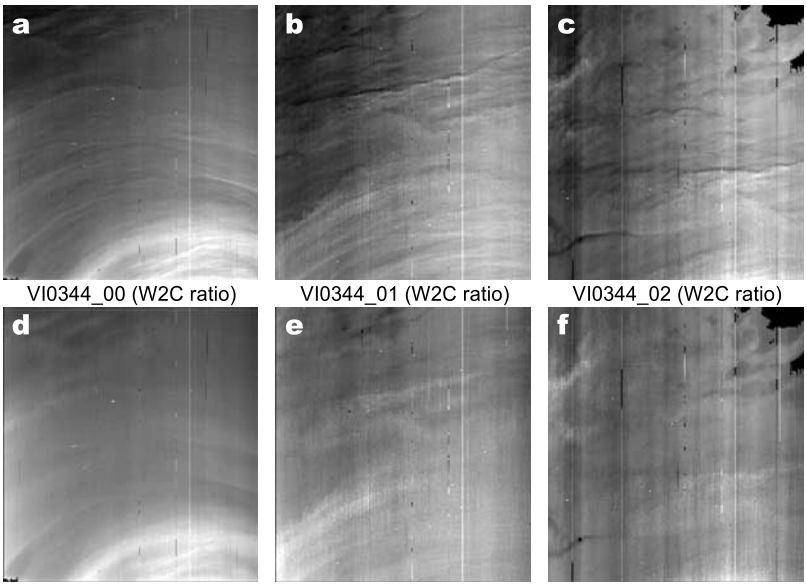

Figure 3. The W2C ratio images from Orbit 344. Figures 3a–3c all exhibit systematic brightening toward the right edge. This may be due to a slight wavelength change (~0.15 nm) from the left edge to the right. Also corrected for is a slight vertical offset which is the cause of relief-like appearances of cloud edges in images Figures 3a–3c. In the corrected Figures 3d–3f, such effects are no longer noticed.

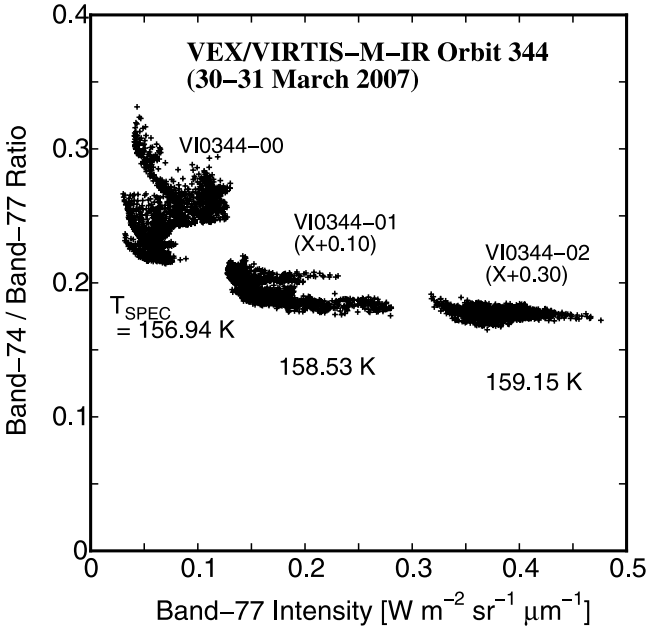

Figure 4. W2C ratios, from three data cubes acquired during the Orbit 344, are plotted against the observed band 77 intensity. Points from VI0344_01 and VI0344_02 are horizontally offset by 0.10 and 0.30 W m^{-2} sr^{-1} μm^{-1}, respectively, so the data from different cubes can easily be compared. The W2C ratio tends to decrease as the spectrograph temperature gets higher, indicating that the temperature-dependent wavelength shift has significant effects on the W2C ratio.

for this effect by applying a small tilt to the spectra, −0.08 band (−0.7 nm) on one end and +0.08 band (+0.7 nm) on another end of a scan. Although the correction is not perfect, most of systematic brightening seen in the "uncorrected" images can be removed. In the following analysis, the corrected data are used.

[14] In Figure 4, we plot the W2C ratio against $I_{1.74\mu m}$. There exist 2 distinct branches in the plot of the VI0344_01 data (Figure 4, middle). These can be characterized as follows: (1) The "main" branch has W2C ratio of ∼0.18, and the ratio increases to ∼0.20 as the $I_{1.74\mu m}$ gets smaller (low-intensity region). (2) The "upper" branch has nearly constant W2C of ∼0.20 for all the range of $I_{1.74\mu m}$.

[15] There are noticeable discrepancies (vertical offsets) between the data from different cubes. These discrepancies may likely be attributed to the shift of observing wavelength due to temperature changes. To assure the internal consistency of data, we use the data from a single cube, VI0344_01, for the analysis.

[16] What we try in the followings is to construct atmospheric models, with fewest free parameters, which can simultaneously reproduce the observed $I_{1.74\mu m}$ and W2C ratio.

3. Model Computations

3.1. Atmospheric Structure and Opacity Sources

[17] Atmospheric structure (pressure/temperature profile) is taken from *Seiff* [1983]. Nominal atmospheric composition of 96.5% CO_2 and 3.5% N_2 as well as the hydrostatic equilibrium are assumed to interpolate values given in the table. The water vapor abundance is assumed to be constant (25 ppm) below 50 km altitude (near the middle of aerosol layers) and its opacity becomes negligible at higher levels [*Taylor et al.*, 1997; *Svedhem et al.*, 2007].

[18] Once the temperature and pressure are specified, the absorption coefficients can be obtained by performing standard line-by-line computations. Our model includes three opacity sources: (1) CO_2 line absorption, (2) H_2O line absorption, and (3) continuum absorption.

[19] Other minor gases are neglected since they only slightly modulate the observed intensity at VIRTIS-M's spectral resolution, ∼0.01 μm. CO_2 line absorption is computed by referring to the Carbon Dioxide Spectroscopy Databank (CDSD; http://spectra.iao.ru). The line shape (Doppler and pressure broadened) is simulated with a Voigt function. We truncate the profile (force the absorption to zero) in the far wing at a distance of 50 times the half width from the line center. H_2O absorption is computed using HITEMP database. Wavelength-independent continuum absorption of the type introduced by *Pollack et al.* [1993] is used in the computations. The strength of this for the 1.74 μm window is 7.0×10^{-9} cm^{-1} $amagat^{-2}$. Rayleigh scattering is neglected as its optical depth for the entire atmospheric column amounts only 0.4 in the 1.74 μm window [*Hansen and Hovenier*, 1974; *Hansen and Travis*, 1974]. Opacities computed for two wavelengths, 1.705 and 1.735 μm, corresponding to a 5 km optical path, are shown as a function of the altitude in Figure 5.

3.2. Aerosol Vertical Distribution

[20] On the basis of direct measurements by descent probes to Venus atmosphere, several distinct layers of aerosol concentration have been identified [*Marov et al.*, 1980; *Ragent and Blamont*, 1980; *Knollenberg and Hunten*, 1980]. (1) Upper haze (UHZ), above 66 km, (2) upper cloud (UCL), 56–66 km, (3) middle cloud (MCL), 50–56 km, (4) lower cloud (LCL), 47–50 km, lower haze (LHZ), below 47 km.

[21] To keep our model simple enough, we set 5 km vertical grids in our model. The first layer starts at the ground surface (z = 0 km) and extends upward to z = 5 km, and the ith layer is between $z_{i,bottom} = (i - 1) \times 5$ km and $z_{i,top} = i \times 5$ km. The topmost layer in our model is the 13th (65–70 km). Anything above this is neglected since neither significant opacity source nor emission source for the 1.74 μm window exists. In doing this, altitude assignments for nominal aerosol layers are as follows (Figure 6): (1) UHZ, 65–70 km, (2) UCL, 55–65 km, (3) MCL, 50–55 km, (4) LCL, 45–50 km, (5) LHZ, 30–45 km.

[22] Within a layer, gaseous opacity, including CO_2, H_2O and continuum, is computed for every 0.1 km (Figure 5) and is subsequently summed over the altitude range (5 km):

$$\tau_{gas} = \int_{z_{bottom}}^{z_{top}} \tau(z)dz. \quad (1)$$

The scale height of aerosols is assumed to be the same as that of the gas within a layer.

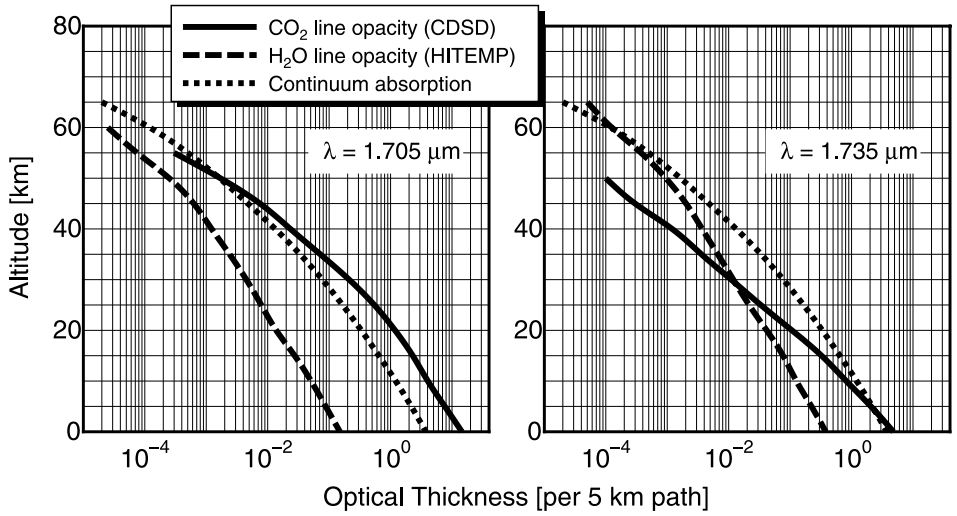

Figure 5. Line absorption opacity (CO_2 and H_2O) as well as the continuum opacity as a function of the altitude from the ground surface are shown. The H_2O abundance is 25 ppm. Note that the continuum absorption (dotted line) is common in two wavelengths, (left) 1.705 μm and (right) 1.735 μm, so the comparison is easy.

3.3. Radiative Transfer Computation

[23] We employ the Discrete Ordinate Radiative Transfer (DISORT) program developed by Stamnes and colleagues [*Stamnes et al.*, 1988]. The single-scattering phase functions for aerosols are approximated using the Henyey-Greenstein analytic function:

$$P_{HG}(\theta) = \frac{1 - g^2}{(1 + g^2 - 2g\cos\theta)^{3/2}}, \qquad (2)$$

where θ is the scattering angle. The anisotropy factor, $-1 \leq g \leq 1$, determines the degree of forward scattering (g is positive) or backward scattering (g is negative). On the basis of a series of Mie computations for Venusian aerosols, with an assumption of sulfuric acid droplets [*Palmer and Williams*, 1973], values of g are found to fall within the range of 0.6$\sim$0.9 in the visible and near-infrared wavelengths.

[24] Because we deal with transmission of infrared radiation which is affected primarily by forward scattering by the aerosols, using a Henyey-Greenstein function with properly adjusted g is just adequate for Venus nightside simulations. For example, the following phase functions are almost identical when used in simulations of the nightside disk emission: (1) A single-peak Henyey-Greenstein function with $g = 0.75$. (2) A combination of forward-scattering and backward-scattering Henyey-Greenstein functions with $g_1 = 0.8$, $g_2 = -0.8$, $f_1 = 0.979$ (yielding an averaged anisotropy factor of 0.75) [*Tomasko et al.*, 1978]. (3) Numerically derived Mie scattering phase functions for mode 2, 2', and 3 particles at 1.74 μm wavelengths (all within the range $0.76 \leq g \leq 0.80$).

[25] An important parameter to control the performance of DISORT computation is the number of streams, NSTR. This parameter determines how radiation field within a layer is decomposed. According to *Levoni et al.* [2001], the amplitude of residual errors, for models with Henyey-Greenstein phase function, converges to $\sim$0 for a choice of NSTR $\geq$ 32. We therefore use NSTR = 32 for our computations with Henyey-Greenstein functions.

4. Computational Results

4.1. Types A–C: Models With Three Cloud Layers

[26] First, we simplify the model by omitting haze layers (UHZ and LHZ) as optically thin hazes may be expected to have minimal effects. We call such a model "type A": In model A1, the optical thickness in UCL is allowed to vary,

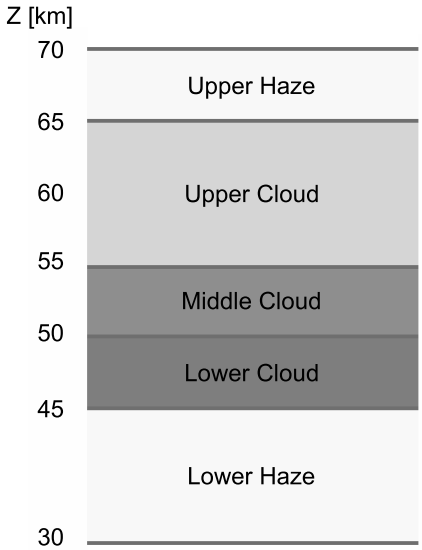

Figure 6. A simplified cloud model in which aerosol layers are organized with vertical resolution of 5 km. According to the atmospheric opacity displayed in Figure 5, location of scattering medium above 50 km altitude is not uniquely determined by this analysis.

Table 2. Cloud Parameters for Model A Series

	Z (km)	g	ω	τ_{A1}	τ_{A2}	τ_{A3}
	65–70					
	60–65					
UCL	55–60	0.75	0.997	variable	5	5
MCL	50–55	0.75	0.997	5	variable	5
LCL	45–50	0.75	0.990	5	5	variable
	40–45					
	35–40					

Table 3. Cloud Parameters for Model B Series

	Z (km)	g	ω	τ_{B1}	τ_{B2}	τ_{B3}
	65–70					
	60–65					
	55–60					
UCL	50–55	0.75	0.997	variable	5	5
MCL	45–50	0.75	0.997	5	variable	5
LCL	40–45	0.75	0.990	5	5	variable
	35–40					

while models A2 and A3 have variable optical thicknesses in MCL and LCL, respectively (Table 2). The initial results indicate the nominal continuum absorption, 7.0×10^{-9} cm^{-1} amagat^{-2}, too strong (Figure 7). It is found that half the nominal value yields models' W2C ratios at the level of observed main branch. We therefore adopt 3.5×10^{-9} cm^{-1} amagat^{-2} in the following computations.

[27] By examining the results shown in Figure 7, it is found that the model is insensitive to the exact location of cloud opacity within 50–60 km altitude range (models A1 and A2). Model 3, on the other hand, exhibits an increase of W2C ratio for low-intensity region, similar to the behavior of observed main branch. This may be suggesting that the main opacity is within the lower part of the clouds, consistent with *Grinspoon et al.*'s [1993] finding. This motivates us to lower the cloud layers by one altitude grid ("type B" models in Table 3). Other parameters remain the same as type A. By comparing the results shown in Figure 8 with Figure 7, we find that model B3 with the variable opacity in LCL (40–45 km) yields the behavior of W2C curve similar to the observed main branch. Through these experiments we believe that it is essential to place in our model the main cloud opacity at $z = 40$–45 km. This is lower than previously proposed altitudes [cf. *Grinspoon et al.*, 1993], however, it should be emphasized that this likely depends on the choice of continuum absorption strength and/or on other adjustables. We therefore may not be sensitive to the "absolute" altitudes of cloud layers. Still, it should be possible to argue, in "relative" sense, how cloud structure differs between the observed main and upper branches.

[28] Now, we examine, on the basis of model B3, how cloud single-scattering albedo affects the results. Variations in this "type C" are shown in Table 4: Table 5

[29] 1. $\omega_{LCL} = 0.970$. A strong-absorption case (may imply a considerable amount of contaminant).

[30] 2. $\omega_{LCL} = 0.990$. The nominal albedo for the LCL particles as obtained from a Mie scattering computation with the mode 3 particle parameters. This value makes the model identical to B3.

[31] 3. $\omega_{LCL} = 0.997$. All the clouds (UCL, MCL, and LCL) have the same "high" single-scattering albedo.

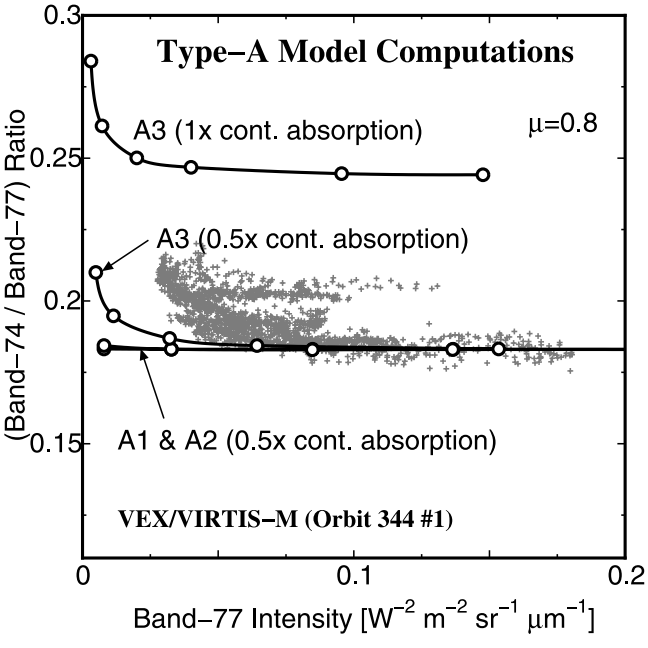

Figure 7. W2C ratios computed with type A models are compared with the observation. The curve for model A3 with the nominal continuum absorption motivates us to half the strength, down to 3.5×10^{-9} cm^{-1} amagat^{-2}. Curves from models A1 and A2 are almost identical, indicating that the location of aerosols within 50–60 km altitude range cannot be precisely determined in this analysis.

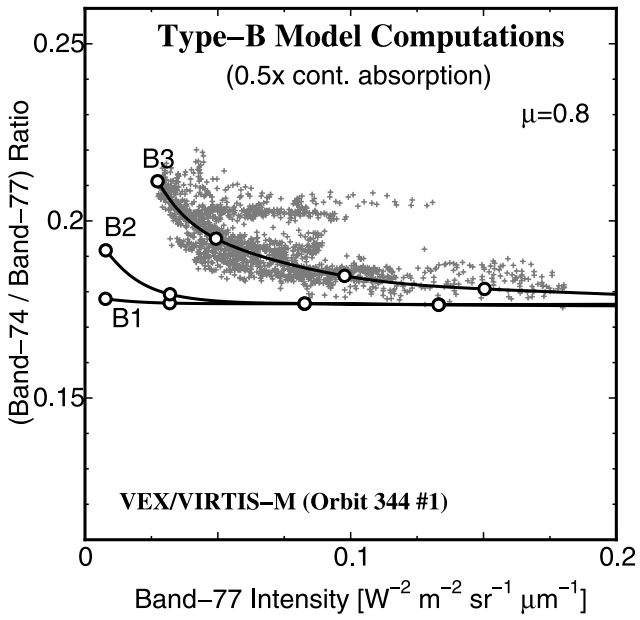

Figure 8. Same as Figure 7 but for type B models (with a slightly different y axis range). The curve from model B3 shows a good agreement with the observed main branch. Curves from B1 and B2 look just similar as those in Figure 7 but slightly lower. This suggests that the main (variable) opacity needs to be located within 40–45 km altitude range.

Table 4. Cloud Parameters for Model C Series

	Z (km)	g	τ	ω_{C1}	ω_{C2}	ω_{C3}
	65–70					
	60–65					
	55–60					
UCL	50–55	0.75	5	0.997	←	←
MCL	45–50	0.75	5	0.997	←	←
LCL	40–45	0.75	variable	0.970	0.990	0.997
	35–40					

[32] The results (Figure 9) show that loci of models C1 and C3 envelop almost all the points in the main branch. This means that the observed variation in W2C ratio could be explained by variation of cloud single-scattering albedo within a range, $0.970 \leq \omega \leq 0.997$. To reproduce the upper branch, single-scattering albedos lower than 0.970 are required. Validity of this model will be discussed in the later section.

4.2. Types D and E: Models With Hazes

[33] In "type D" models, we introduce a layer of small aerosols (LHZ) at an altitude range 30–40 km, just below the LCL of model C2 (= B3). The anisotropy factor (g = 0.65) and the single-scattering albedo (ω = 0.997) are those obtained for mode 1 particles through Mie scattering computation. The optical thickness of LHZ is allowed to vary and 3 different values, 1, 2, and 4, are tested (Table 4). The results shown in Figure 10 are surprising because a small amount of opacity introduced below the cloud base significantly lower the model's W2C ratio.

[34] Then, we include both lower and upper hazes in the model ("type E"). An upper haze layer (ω = 0.997 and g = 0.65) is added to models D1–D3. The optical thickness for the upper haze is fixed to τ_{UHZ} = 5. This value is chosen arbitrarily because the purpose of type E models are just to know how upper haze could affect the model intensities and W2C ratios. Model parameters are summarized in Table 6 and the results shown in Figure 11.

[35] These models do not significantly improve type D models. Probably, the horizontal portion of the locus may be slightly closer to the observations than type D models. To summarize the models A through E, there seems to be many ways of reproducing the main branch. On the other hand, none of these models can reproduce the upper branch. Recall that we halved the strength of continuum absorption by just referring to the initial results of type A model computation (Figure 7). We now believe that more continuum absorption is needed, probably between the nominal strength and a half of it. So we are motivated to adjust the continuum absorption again.

Table 5. Cloud Parameters for Model D Series

	Z (km)	g	ω	τ_{D1}	τ_{D2}	τ_{D3}
	65–70					
	60–65					
	55–60					
UCL	50–55	0.75	0.997	5	←	←
MCL	45–50	0.75	0.997	5	←	←
LCL	40–45	0.75	0.990	variable	←	←
LHZ	30–40	0.65	0.997	1	2	4

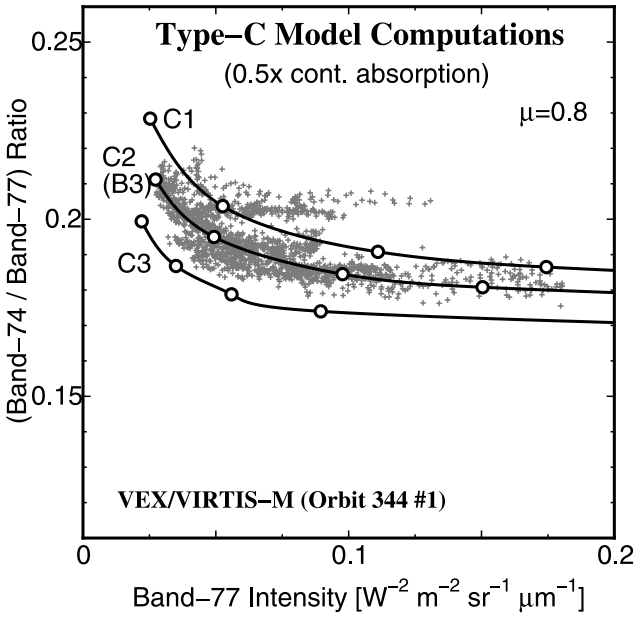

Figure 9. Same as Figure 8 but for type C models. The model C2 is identical with B3. Models C1 and C3 envelope the observed main branch. The upper branch, on the other hand, cannot be reproduced unless very low ω_{LCL} is assumed.

4.3. Type F: Models With More Continuum Absorption

[36] We have readjusted the continuum absorption to 5.6×10^{-9} cm^{-1} amagat^{-2}, 80% of the value of *Pollack et al.*

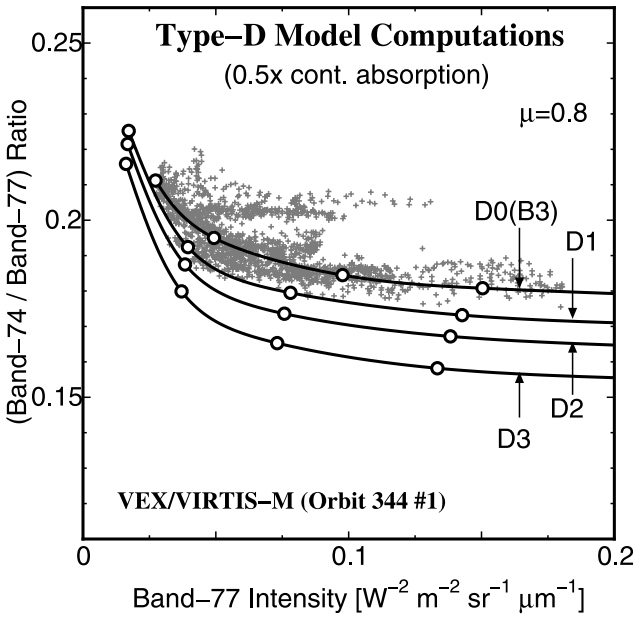

Figure 10. Same as Figure 8 but for type D models. The model D0 is identical with C2 and B3. It is surprising that only a small amount of aerosol opacity introduced in 30–40 km altitude range substantially lowers the model's W2C ratio.

Table 6. Cloud Parameters for Model E Series

	Z (km)	g	ω	τ_{E1}	τ_{E2}	τ_{E3}
	65–70					
	60–65					
UHZ	55–60	0.65	0.997	5	←	←
UCL	50–55	0.75	0.997	5	←	←
MCL	45–50	0.75	0.997	5	←	←
LCL	40–45	0.75	0.990	variable	←	←
LHZ	30–40	0.65	0.997	1	2	4

[1993]. The new value is so chosen that the model E1, without changing the aerosol parameters, can fit the observed upper branch. This model, "type F1" ($\tau_{LHZ} = 1$), is plotted in Figure 12 and matches nicely to the right half of the upper branch. After adjustment of the continuum absorption, model F2 (the same parameters as E2) is found to reproduce the left half of the upper branch. We have found that model F3 (from E3) with $\tau_{LHZ} = 4$ reproduces the upper edge of the main branch. Additionally, we have constructed the model F4 with $\tau_{LHZ} = 8$ which traces the lower edge of the main branch.

[37] On each locus in Figure 12, total aerosol optical thickness (35, 40, 47, and 55) is marked. This is the sum of optical thicknesses in UHZ, UCL, MCL, LCL, and LHZ and no gaseous opacity is included. As first three are fixed to 5 (Table 7), τ_{LCL} is given as $\tau_{LCL} = \tau_{total} - 15 - \tau_{LHZ}$.

[38] These "type F" models are favored as the observation can be explained with a minimal number of variables. To explain the observed intensity variation, the optical thickness of the lower cloud (τ_{LCL}) plays the key role. However, by varying only the LCL opacity, we obtain just one locus as seen in Figure 12. To jump from one locus to another, we need to change the lower haze opacity in the range $1 \leq \tau_{LHZ} \leq 8$. We conclude that this is the simplest model which can reasonably explain the observations.

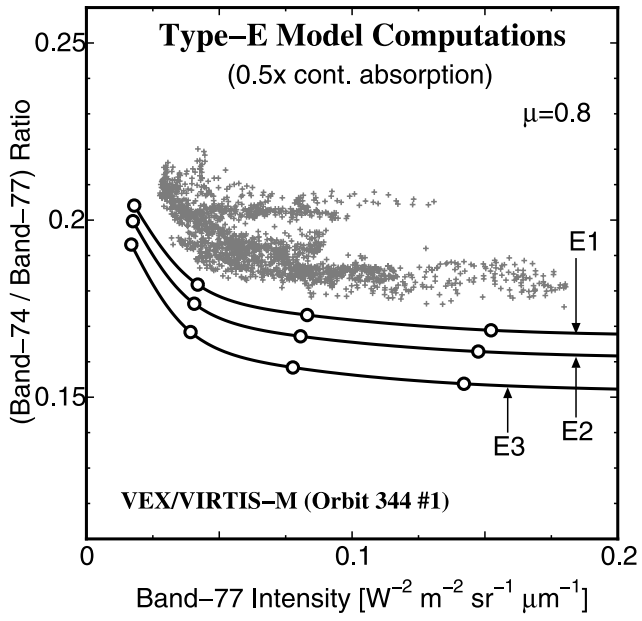

Figure 11. Same as Figure 8 but for type E models. Adding the upper haze (55–60 km altitude) only slightly lowers the model's W2C ratio.

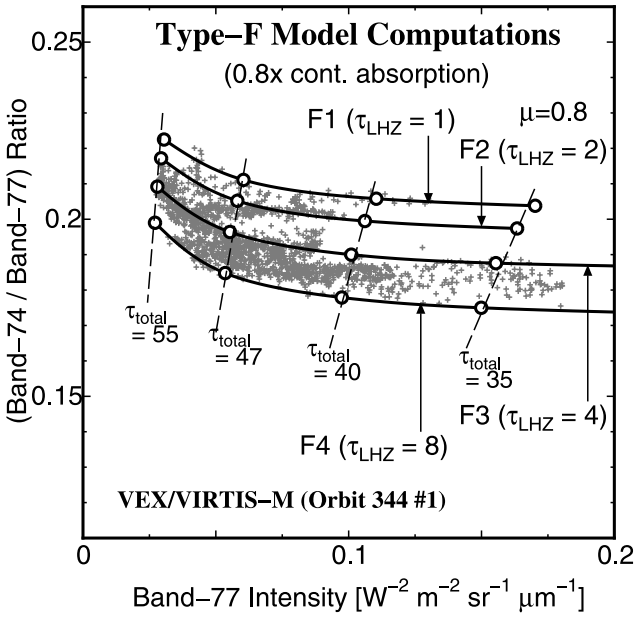

Figure 12. Same as Figure 11 but after adjusting the continuum absorption to 5.6×10^{-9} cm^{-1} amagat^{-2}. The model E1 (Figure 11) becomes F1 and E2 becomes F2. Both models reproduce the observed upper branch well. The model E3 becomes F3 and traces the upper edge of the main branch. The lower edge is traced with model F4 ($\tau_{LHZ} = 8$).

5. Discussion

5.1. Comparison Between Type C and Type F Models

[39] We compare models C1–C3 with models F2–F4. The former explains variation of W2C ratio with variation of aerosol single-scattering albedo, while the latter with variation of subcloud aerosol opacity.

5.1.1. Limb Darkening on the Nightside Disk

[40] In Figure 13, the limb-darkening curves for models C3 and F4 are compared with an empirical linear approximation derived by *Carlson et al.* [1991], $I(\mu)/I(\mu = 1.0) = 0.316 + 0.685\mu$ (open circles). Both cloud models yield the limb-darkening curves (C3 and F4 nearly identical) which are in an excellent agreement with *Carlson et al.*'s [1991] approximation. Assuming such an approximation is valid for VEX/VIRTIS data acquired 17 years after Galileo/NIMS data, it can be concluded that models C3 and F4 are equally

Table 7. Cloud Parameters for Model F Series

	Z (km)	g	ω	τ_{F1}	τ_{F2}	τ_{F3}	τ_{F4}
	65–70						
	60–65						
UHZ	55–60	0.65	0.997	5	←	←	←
UCL	50–55	0.75	0.997	5	←	←	←
MCL	45–50	0.75	0.997	5	←	←	←
LCL	40–45	0.75	0.990	variable	←	←	←
LHZ	30–40	0.65	0.997	1	2	4	8

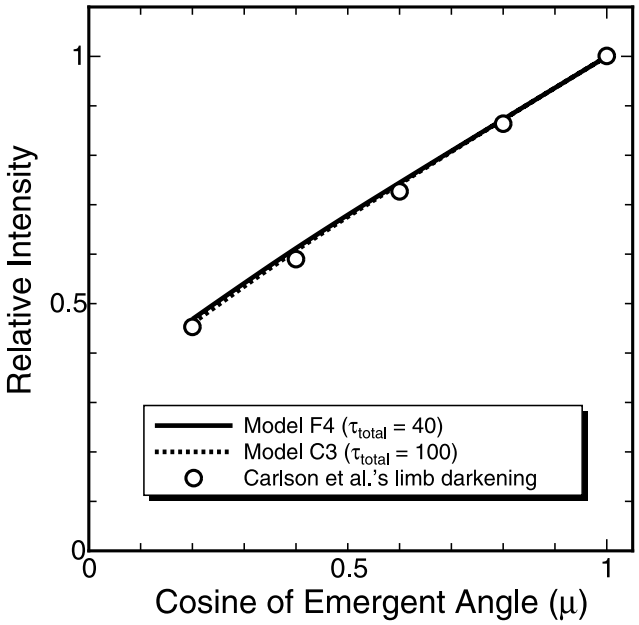

Figure 13. Limb-darkening curves for the 1.74 μm nightside emission computed with model F4 (solid line) and C3 (dotted line). Computed intensities are plotted against cosine of the emergent angle (μ) after normalized to the disk center ($\mu = 1.0$) intensity. Also shown (open circles) is *Carlson et al.*'s [1991] linear approximation derived for the Galileo/NIMS observation (see text).

good to reproduce the limb-darkening curves observed on the nightside of Venus in the 1.74 μm window.

5.1.2. Reflectivity on the Dayside Disk

[41] When applying the same models to the dayside disk, it should be reminded that a "single-peak" Henyey-Greenstein function used in our models has limitations. As described in section 3.3, phase functions with similar anisotropy g behave almost identical in the nightside simulations. On the other hand, they yield substantial differences in reflectivities (a factor $\sim$2 at $\mu = 0.5$) when used in simulations of the dayside reflectivities. Therefore, we may only be able to compare "differences" (or contrast) in reflectivities of different models.

[42] Total aerosol opacities are adjusted as follows: $\tau_{total} = 30$ for model C1, 45 for C2, 70 for C3, and $\tau_{total} = 40$ for models F2, F3, and F4, in order that the models give simulated nightside emission $I_{1.74\mu m} \sim 0.1$ W m^{-2} sr^{-1} μm^{-1}. Then, the models are used to compute the intensity distribution across the dayside disk (Figure 14). Curves for type C models are normalized to the peak intensity of model C3 curve (at $\mu = 1.0$). Curves for type F models are represented by the model F4 curve as other two (F2 and F3) are just identical in their shapes and also the absolute values with F4.

[43] It is found that type C models predict substantial contrast up to 20% between C1 and C3, while type F models allow no noticeable contrast on the dayside disk. Such high contrast markings on the dayside disk at 1.74 μm have not been reported. Examinations of VIRTIS 1.74 μm images acquired with a shorter exposure time (0.02 s) also seem to support "featureless" dayside disk of Venus. Therefore, it can be concluded that type F models are more favored than type C.

5.2. Optical Properties of the Lower Haze

5.2.1. Single-Scattering Albedo

[44] One of constraints on the subcloud haze we have obtained is high single-scattering albedo. To be influential on the W2C ratio (Figure 12), the subcloud haze particles should allow radiation they scatter to continue traveling in the atmosphere. Then, en route an extended path due to scattering, the radiation would be more attenuated by the gaseous absorption at 1.71 μm than at 1.74 μm, resulting in a higher contrast between 2 bands (or, in other words, lower W2C ratio). Lowering the subcloud haze albedo results in higher W2C ratio, the same effect as obtained by increasing the wavelength-independent continuum absorption. Our value $\omega = 0.997$ well compares to those by *Ekonomov et al.* [1983]: the single-scattering albedo in the altitudes 15–48 km is 0.9986 at a wavelength 0.726 μm (Venera 11) and 0.9969 at 0.634 μm (Venera 12).

5.2.2. Anisotropy of Single Scattering

[45] The anisotropy of the scattering phase function allows a similar insight. With strongly forward-scattering aerosols (i.e., larger g), scattered radiation may propagate in nearly the same direction as before the scattering. This causes just minimal increase in the traveling light path. In contrast, weakly forward-scattering aerosols (smaller g) make the radiation more "scattered." This makes the light path much longer than the case of strongly forward-scattering aerosols, resulting in greater attenuation of radiation.

[46] To strengthen the case, an additional test with "type G" models is performed (Figure 15). The anisotropy factor, g, is decreased to 0 [*Ekonomov et al.*, 1983], making the

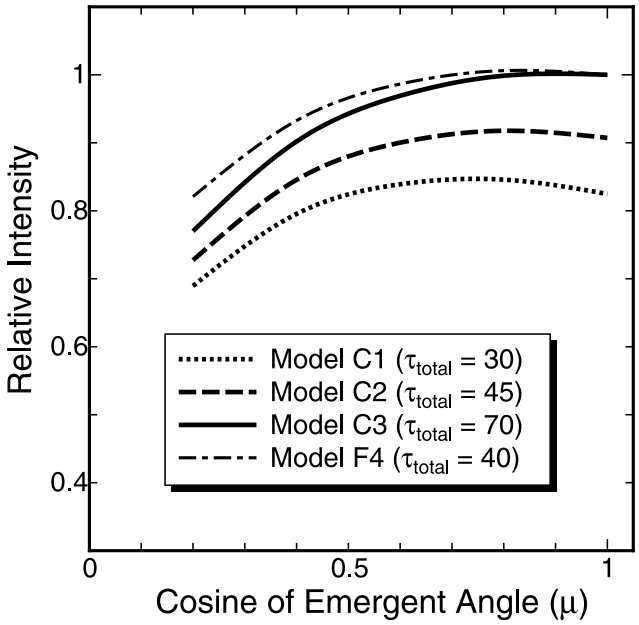

Figure 14. Limb-darkening curves of the reflected sunlight on the dayside disk at 1.74 μm computed with type C and type F models. Curves for models C1–C3 are normalized to model C3's disk center brightness. Models F2–F4 are represented by the curve for model F4 as they are all identical with each other (normalized to model F4's disk center brightness). Note the large contrast predicted by models C1–C3 for the dayside disk.

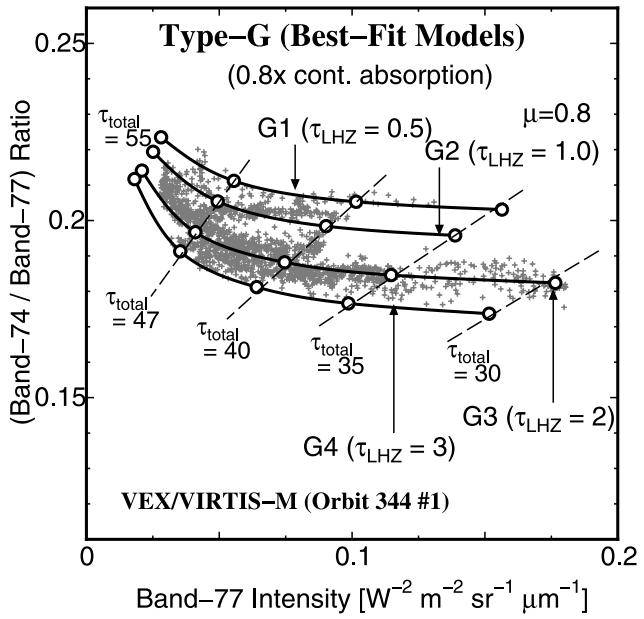

Figure 15. Same as Figure 12 but with "isotropically scattering" lower haze (g = 0 for the scattering phase function). This model requires smaller optical thicknesses, compared to models F1–F4, for the lower haze ($\tau_{LHZ} = 0.5 \sim 3$) and for the lower cloud ($\tau_{total} = 30 \sim 50$). These models seem to be consistent with previous probe measurements and, therefore, are favored as the best-fit models.

subcloud aerosols isotropically scattering to mimic extremely fine particles. All other parameters remain unchanged from type F models. The results same as shown in Figure 12 can be obtained by models with smaller optical thicknesses for the lower haze (τ_{LHZ}) and for the lower cloud (τ_{LCL}). We find the following:

[47] 1. Observed W2C ratios can be explained with smaller lower haze opacity, $\tau_{LHZ} \leq 3$. This is in a better agreement with small optical thicknesses ($\tau \sim 3$) inferred from Venera probe measurements [*Marov et al.*, 1980].

[48] 2. The range of observed intensities, $I_{1.74\mu m}$, can be explained with the total aerosol opacity of approximately 30–50. This does not seem to be too far from previously suggested range, 25–35 for the visible wavelengths [*Ekonomov et al.*, 1983].

[49] The observations seem to support smaller anistropy (and higher single-scattering albedo) for the subcloud haze which may imply concentration of fine particles although it is not all that simple to infer, from only g values, the actual particle size. We now conclude that the best-fit model is type G.

5.3. Lower Haze Opacity Maps and Their Implications

[50] Now we map the lower haze opacity (τ_{LHZ}) using type G models. It is found that the four curves in Figure 15 can reasonably be approximated by

$$W2C = 0.28 + C \times \left[\exp\left(-\frac{I_{1.74\mu m} + 0.005}{0.023}\right) - 1\right], \quad (3)$$

where C is 0.075, 0.084, 0.096, and 0.106 for models G1 (τ_{LHZ} = 0.5), G2 (1.0), G3 (2.0), and G4 (3.0), respectively. By inverting this, we can map C values over an image frame. Then, the lower haze opacity (τ_{LHZ}) can be obtained as follows:

$$\tau_{LHZ} = \left(\frac{C - 0.054}{0.030}\right)^2. \quad (4)$$

A grayscale map of τ_{LHZ} for VI0344_01 data is compared with the 1.74 μm image in Figure 16.

[51] Variability of τ_{LHZ} in the derived map is substantial, from almost 0 to ~4 (Figure 16). This can be compared with previous probe measurements. In the Pioneer Venus probe experiments, the nephelometer (Day probe) and LCPS (Large probe) detected the lower haze. Because the nephelometer's lower limit of detection is ~2 orders of magnitude higher than LCPS, the lower haze at the Day probe site had 2 orders of magnitude stronger backscatter (at 900 nm) than at the Large probe site. The great spatial variability we have obtained seems to be consistent with this. Note that a large area of low τ_{LHZ} (labeled *f*), south of approximately 40°S latitude, corresponds to the upper branch in the W2C–$I_{1.74\mu m}$ plot.

[52] The lower haze opacity basically anticorrelates with the 1.74 μm intensity. Locations indicated with labels *c* and *e* are dark in $I_{1.74\mu m}$ and have higher τ_{LHZ} (up to ~4). This anticorrelation may imply that subcloud aerosols provide condensation nuclei for the lower cloud. There are, however, some exceptions. A dark band (*b*) seen in $I_{1.74\mu m}$ does not have a counterpart in the τ_{LHZ} map. The same is true for dark features near the image center (*d*). Such features may, therefore, be produced by local temperature fluctuations caused by some sort of waves.

[53] There is one place where high $I_{1.74\mu m}$ corresponds to large τ_{LHZ} (labeled *a*). We think this very important. This may imply that penetration of sunlight through the clouds triggers a chain of photochemical reactions, producing subcloud aerosols in less cloudier regions. One of such hypothesis has been proposed by *Yung and Liang* [2008]. We discuss possible composition of the subcloud haze later.

5.3.1. Examining Other VIRTIS Data

[54] We have examined additional data to find more cases that exhibit positive correlations between $I_{1.74\mu m}$ and τ_{LHZ}.

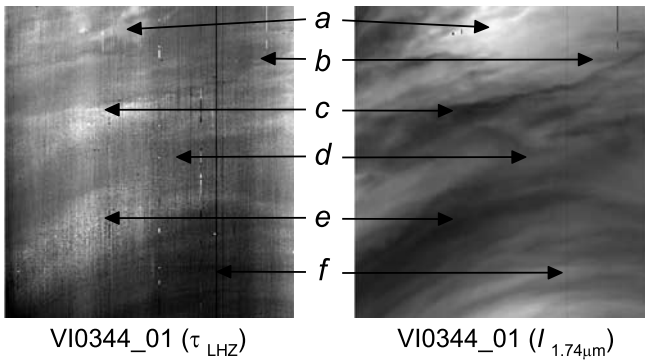

Figure 16. A map of (left) lower haze opacity is compared with (right) 1.74 μm image. The lower haze opacity basically anticorrelates with the 1.74 μm intensity with some exceptions, such as those labeled *a*, *b*, and *d* (see text).

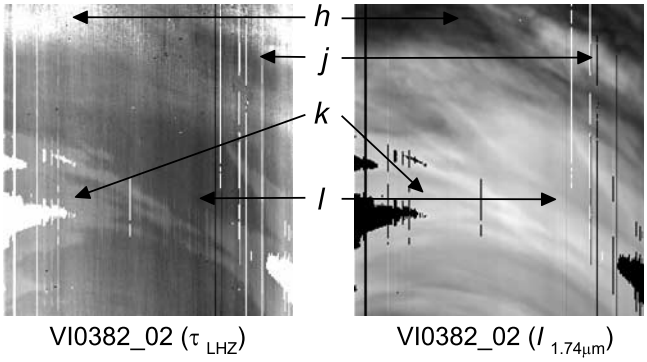

Figure 17. Same as Figure 16 but for VI0382_02 data cube. Normal regions (*h* and *j*) exhibit anticorrelations between τ_{LHZ} and $I_{1.74\mu\mathrm{m}}$. A large area of positive correlation, surrounded by sharp edges, exists (labeled *k*). Note that saturated pixels are blacked out on the right and appear white on the left.

There are only seven orbits during which VIRTIS data were acquired with 18 s exposures. Among those, we have found a very interesting feature in VI0382_2 cube (Orbit 382, 07–08 May 2007). A grayscale map of τ_{LHZ} for this cube is compared with the 1.74 μm image in Figure 17. The latitude range is from ~65°S (bottom edge of the map) to ~23°S (top edge), similar to that of VI0344_01 (Table 1).

[55] A large area, with sharp edges, of enhanced τ_{LHZ} is obvious (labeled *k*). Inside of this area appears rather flat in spite of the fact that the $I_{1.74\mu\mathrm{m}}$ map indicates cloud opacity variations in it. If the area corresponds to where production of subcloud aerosols is enhanced owing to penetration of incident sunlight, it may be expected to find more aerosols when observed in the day. We speculate that the observation by nephelometer on board Pioneer Venus Day probe was made in one of such regions (the probe descended the atmosphere at ~30°S, not too far from the latitude of this feature).

[56] Labels *h* and *j* indicate "normal" regions where the anticorrelation between τ_{LHZ} and $I_{1.74\mu\mathrm{m}}$ is seen. No systematic decrease of lower haze opacity toward the south pole is observed in this map, very different from that is shown in Figure 16. Temporal and spatial variability is therefore substantial.

5.3.2. Atmospheric Circulation and the Lower Haze

[57] The fact that τ_{LHZ} only weakly correlates with the 1.74 μm intensity may imply that the dynamical coupling between the lower cloud and the subcloud haze is not strong. This is not surprising because, in the probe measurements [*Tomasko*, 1983], the altitude range 31–48 km is considered "stable" (i.e., the measured temperature lapse rate dT/dz is larger than the adiabatic lapse rate Γ). In such a region, a upwelling motion that an air parcel gets when it is heated will soon be suppressed because the air parcel cools down with a rate larger than the lapse rate of its surroundings.

[58] *Schubert* [1983] proposed a hypothesis of several (vertically stratified) circulation cells in Venus atmosphere. One within the cloud layer (50–70 km altitude) which is directly driven by absorption of the solar energy by the clouds. Another direct cell is in the lowermost atmosphere which is driven by absorption of the solar energy by the ground. This cell is expected to extend up to ~40 km altitude. Between two direct cells (40–50 km altitude) is an indirect cell frictionally driven by direct cells above and below it. The wind directions (alternating equatorward and poleward) measured by the Pioneer Venus probes [*Counselman et al.*, 1980] in the middle-to-lower atmosphere are consistent with this hypothesis.

[59] According to Schubert's proposal, equatorward motion is expected for the altitude ~50 km near the lower limb of the direct cell. On the other hand, poleward motion is expected for the altitude ~40 km near the lower limb of the indirect cell. It should therefore be of great interest to track the meridional motion of features in the lower cloud and in the lower haze.

5.4. Possible Composition of Subcloud Haze

[60] Very little is known to date about the composition of the subcloud aerosols. *Golovin and Ustinov* [1982] analyzed spectrophotometric data obtained from Venera 9–12 and have constrained some properties of subcloud aerosols. They have found that the particles are small (0.05–0.1 μm radii) and are mainly in altitudes above 30 km. They also note detection of some larger particles (0.1–0.3 μm) detected at Venera-12 landing site. Refractive index has only crudely been constrained to $n \leq \sim 1.8$ by attenuation effectiveness factor measured by Venera 12 for larger (0.2–0.3 μm) particles. They listed a variety of candidate species, such as chlorine-containing salts (KCl, NaCl, $MgCl_2$, $PbCl_2$, etc.), Pb, $PbBr_2$, PbS, PbO, Zn and some others.

[61] Other possible candidates for the lower haze are H_2SO_4 plus some contaminants as proposed by *Esposito et al.* [1983] and $Fe_2(SO_4)_3$ proposed by *Krasnopolsky* [1985]. Neither of these as well as those listed by *Golovin and Ustinov* [1982] has been confirmed to date.

[62] Recently, *Yung and Liang* [2008] proposed that sulfur atoms and molecules (up to S_8) are produced from OCS by photosensitized dissociation processes in the 30 km region. Such processes may significantly reduce OCS in the lower atmosphere, consistent with the observed OCS vertical profile. Polymeric and alpha-sulfur, products of such processes, are nonabsorbing at 1.7 and 2.3 μm, and thus may be good candidates for the subcloud aerosols. Increases of τ_{LHZ} found for regions *a* (Figure 16) and *k* (Figure 17), where overlying clouds are thinner, may support this hypothesis. Another support to this comes from *Bertaux et al.* [1986]. They analyzed the absorption spectrum in the ultraviolet obtained from spectrometers on board Vega 1 and 2 and have found that the principal absorbent in the subcloud region is S_8 allotrope of sulfur in the gas phase, with mixing ratios of several to a few tens of ppm.

[63] Although the composition of subcloud aerosols remain unclear at this moment, continuous mapping/monitoring (as demonstrated here) and detailed analysis of high-resolution spectroscopy (lower atmosphere chemistry), combined with laboratory measurements and theories would improve our knowledge on this.

6. Conclusions

[64] We have developed a new method of constraining Venus cloud structure in the middle-to-lower atmosphere

based on analysis of nightside emission in the 1.74 μm window. Ratios of intensities at 2 spectral bands, one at the window center ($\sim$1.74 μm) and another off center ($\sim$1.71 μm), are found to be affected by the distribution and properties in the lower cloud and haze. This method may make it possible to map variations in the horizontal distribution of the lower haze with the remote sensing data. Owing to limitations of our current knowledge on gaseous absorptions (line shapes, line mixings, collision-induced continuum absorption, etc.), determining absolute values for the lower haze parameters is needless to say difficult. The analysis in this paper finds variation in the W2C ratio within a single VIRTIS data cube, VI0344_01 (30–31 March 2007), so we feel confident that the best explanation is spatial variability of aerosol distribution in the lower atmosphere.

[65] The data favor models with shiny and nearly isotropically scattering particles (i.e., very small in size) for the lower haze of which composition is to date quite uncertain. The subcloud haze plays a key role, together with the lower cloud, to explain remarkable variations in the observed W2C ratios and the 1.74 μm intensities. The range of optical thickness found for the lower haze ($\tau_{\mathrm{LHZ}} \sim 0.5$–3) is consistent with the Venera probe measurements [*Marov et al.*, 1980]. The total aerosol optical thickness is found to be in the range 30–50, also not too far from the typical range, 25–35, inferred from in situ solar-radiation flux measurements [*Ekonomov et al.*, 1983].

[66] The question is how stable or unstable these variations of the lower cloud/haze are. It is at this moment unclear how variabilities of aerosols in the middle-to-lower atmosphere are related (or unrelated) to the atmospheric circulations. As this study is the first demonstration of mapping the lower haze distribution using VEX/VIRTIS remote sensing data, further monitoring observations, combined with measurements of trace gas species in the lower atmosphere, would greatly contribute to understandings on the current status and physics/chemistry in this hidden world.

[67] **Acknowledgments.** We are grateful to Robert Carlson and Colin Willson for very useful discussion about the Venus aerosol properties and distributions. Thanks go to Bruno Bezard for providing his analysis on the "spectral shift" of VIRTIS. Dima Titov kindly gave us comments which are of great value to improve our analysis. The VEX/VIRTIS project has been made possible by all-out support from ASI and CNES. T.S. is one of the Interdisciplinary Scientists (IDS) to Venus Express mission and is grateful to ESA for providing such a great opportunity.

References

Allen, D., and J. Crawford (1984), Discovery of cloud structure on the dark side of Venus, *Nature*, *307*, 222–224.

Bertaux, J.-L., et al. (1986), Active spectrometry of the ultraviolet absorption within the Venus atmosphere, *Sov. Astron. Lett., Engl. Transl.*, *12*(1), 33–36.

Carlson, R. W., and F. W. Taylor (1993), The Galileo encounter with Venus: Results from the Near-Infrared Mapping Spectrometer, *Planet. Space Sci.*, *41*, 475–476.

Carlson, R. W., et al. (1991), Galileo infrared imaging spectroscopy measurements at Venus, *Science*, *235*, 1541–1548.

Counselman, C. C., III, A. A. Gourevitch, R. W. King, and G. B. Loriot (1980), Zonal and meridional circulation of the lower atmosphere of Venus determined by radio interferometry, *J. Geophys. Res.*, *85*, 8026–8030.

Crisp, D., and D. Titov (1997), The thermal balance of the Venus atmosphere, in *Venus: Geology, Geophysics, Atmosphere, and Solar Wind Environment*, edited by S. W. Bougher et al., pp. 353–384, Univ. of Ariz. Press, Tucson.

Drossart, P., et al. (2007), A dynamic upper atmosphere of Venus as revealed by VIRTIS on Venus Express, *Nature*, *450*, 641–645.

Ekonomov, A. P., Yu. M. Golovin, V. I. Moroz, and B. Ye. Moshkin (1983), Solar scattered radiation measurements by Venus probes, in *Venus*, edited by D. M. Hunten et al., pp. 632–649, Univ. of Ariz. Press, Tucson.

Esposito, L. W., R. G. Knollenberg, M. Ya. Marov, O. B. Toon, and R. P. Turco (1983), The clouds and hazes of Venus, in *Venus*, edited by D. M. Hunten et al., pp. 484–564, Univ. of Ariz. Press, Tucson.

Esposito, L. W., J.-L. Bertaux, V. Krasnopolsky, V. I. Moroz, and L. V. Zasova (1997), Chemistry of lower atmosphere and clouds, in *Venus: Geology, Geophysics, Atmosphere, and Solar Wind Environment*, edited by S. W. Bougher et al., pp. 415–458, Univ. of Arizona Press, Tucson.

Golovin, Yu. M., and E. A. Ustinov (1982), Subcloud aerosol on Venus, *Cosmic Res.*, *20*, 104–110.

Grinspoon, D. H., et al. (1993), Probing Venus's cloud structure with Galileo NIMS, *Planet. Space Sci.*, *41*, 515–542.

Hansen, J. E., and J. W. Hovenier (1974), Interpretation of the polarization of Venus, *J. Atmos. Sci.*, *31*, 1137–1160.

Hansen, J. E., and L. D. Travis (1974), Light scattering in planetary atmospheres, *Space Sci. Rev.*, *16*, 527–610.

Kamp, L. W., and F. W. Taylor (1990), Radiative transfer models of the night side of Venus, *Icarus*, *86*, 510–529.

Kamp, L. W., F. W. Taylor, and S. B. Calcutt (1988), Structure of Venus atmosphere from modelling of night side infrared spectra, *Nature*, *336*, 360–362.

Kawabata, K., D. L. Coffeen, J. E. Hansen, W. A. Lane, M. Sato, and L. D. Travis (1980), Cloud and haze properties from Pioneer Venus polarimetry, *J. Geophys. Res.*, *85*, 8129–8140.

Knollenberg, R. G., and D. M. Hunten (1980), Microphysics of the clouds of Venus: Results of the Pioneer Venus particle size spectrometer experiment, *J. Geophys. Res.*, *85*, 8039–8058.

Krasnopolsky, V. A. (1985), Chemical composition of Venus clouds, *Planet. Space Sci.*, *33*, 109–117.

Levoni, C., E. Cattani, M. Cervino, R. Guzzi, and W. Di Nicolantonio (2001), Effectiveness of the MS-method for computation of the intensity field reflected by a multi-layer plane-parallel atmosphere, *J. Quant. Spectrosc. Radiat. Transfer*, *69*, 635–650.

Marov, M. Ya., V. E. Lystsev, V. N. Lebedev, N. L. Lukashevich, and V. P. Shari (1980), The structure and microphysical properties of the Venus clouds: Venera 9, 10, and 11 data, *Icarus*, *44*, 608–639.

Palmer, K. F., and D. Williams (1973), Optical constants of sulfuric acid: Application to the clouds of Venus?, *Appl. Opt.*, *14*, 208–219.

Piccioni, G., et al. (2007), South-polar features on Venus similar to those near the north pole, *Nature*, *450*, 637–640.

Pollack, J. B., et al. (1993), Near-infrared light from Venus' nightside: A spectroscopic analysis, *Icarus*, *103*, 1–42.

Ragent, B., and J. Blamont (1980), Structure of the clouds of Venus: Results of the Pioneer Venus nephelometer experiment, *J. Geophys. Res.*, *85*, 8089–8105.

Sato, M., L. D. Travis, and K. Kawabata (1996), Photopolarimetry analysis of the Venus atmosphere in polar regions, *Icarus*, *124*, 569–585.

Schubert, G. (1983), General circulation and the dynamical state of the Venus atmosphere, in *Venus*, edited by D. M. Hunten et al., pp. 681–765, Univ. of Ariz. Press, Tucson.

Seiff, A. (1983), Models of Venus's atmospheric structure, in *Venus*, edited by D. M. Hunten et al., pp. 1045–1048, Univ. of Ariz. Press, Tucson.

Sill, G. T. (1972), Sulfuric acid in the Venus clouds, *Comm. Lunar Planet. Lab.*, *9*, 191–198.

Stamnes, K., S.-C. Tsay, W. Wiscombe, and K. Jayaweera (1988), Numerically stable algorithm for discrete-ordinate-method radiative transfer in multiple scattering and emitting layered media, *Appl. Opt.*, *27*, 2502–2509.

Svedhem, H., et al. (2007), Venus Express: The first European mission to Venus, *Planet. Space Sci.*, *55*, 1636–1652.

Taylor, F. W., D. Crisp, and B. Bezard (1997), Near-infrared sounding of the lower atmosphere of Venus, in *Venus: Geology, Geophysics, Atmosphere, and Solar Wind Environment*, edited by S. W. Bougher et al., pp. 325–351, Univ. of Ariz. Press, Tucson.

Tomasko, M. G. (1983), The thermal balance of the lower atmosphere of Venus, in *Venus*, edited by D. M. Hunten et al., pp. 604–631, Univ. of Ariz. Press, Tucson.

Tomasko, M. G., R. A. West, and N. D. Castillo (1978), Photometry and polarimetry of Jupiter at large phase angles: 1. Analysis of imaging data of a prominent belt and a zone from Pioneer 10, *Icarus*, *33*, 558–592.

Toon, O. B., B. Ragent, D. Colburn, J. Blamont, and C. Cot (1984), Large, solid particles in the clouds of Venus: Do they exist?, *Icarus*, *57*, 143–160.

Young, A. T., and L. D. G. Young (1973), Comments on the composition of the Venus cloud tops in light of recent spectroscopic data, *Astrophys. J.*, *179*, 39–43.

Yung, Y., and M. Liang (2008), Chemical sources and sinks of OCS in the lower atmosphere and on the surfaces of Venus, paper presented at General Assembly 2008, Eur. Geosci. Union, Vienna, 13–18 Apr.

P. Drossart, LESIA, Observatoire de Paris, F-92195 Meudon, France.

G. L. Hashimoto, Laboratory for Earth and Planetary Atmospheric Science, Organization of Advanced Science and Technology, Kobe University, 1-1 Rokkodai-cho, Nada-ku, Kobe 657-8501, Japan.

T. Imamura and T. Satoh, Space Plasma Physics Department, Institute of Space and Astronautical Science, Japan Aerospace Exploration Agency, 3-1-1 Yoshinodai, Sagamihara, Kanagawa 229-8510, Japan. (satoh@stp.isas.jaxa.jp)

N. Iwagami, K. Mitsuyama, and S. Sorahana, Department of Earth and Planetary Science, Graduate School of Science, Tokyo University, 7-3-1 Hongo, Bunkyo-ku, Tokyo 113-0033, Japan.

G. Piccioni, INAF, Istituto di Astrofisica Spaziale e Fisica Cosmica, I-00133 Rome, Italy.